communications earth & environment

ARTICLE

https://doi.org/10.1038/s43247-021-00120-y OPEN

A shift in the ocean circulation has warmed the subpolar North Atlantic Ocean since 2016

Damien Desbruyères[1]✉, Léon Chafik[2] & Guillaume Maze[1]

The Subpolar North Atlantic is known for rapid reversals of decadal temperature trends, with ramifications encompassing the large-scale meridional overturning and gyre circulations, Arctic heat and mass balances, or extreme continental weather. Here, we combine datasets derived from sustained ocean observing systems (satellite and in situ), idealized observation-based modelling (advection-diffusion of a passive tracer), and a machine learning technique (ocean profile clustering) to document and explain the most-recent and ongoing cooling-to-warming transition of the Subpolar North Atlantic. Following a gradual cooling of the region that was persisting since 2006, a surface-intensified and large-scale warming sharply emerged in 2016 following an ocean circulation shift that enhanced the northeastward penetration of warm and saline waters from the western subtropics. The long ocean memory of the Subpolar North Atlantic implies that this advection-driven warming is likely to persist in the near-future with possible implications for the Atlantic multidecadal variability and its global impacts.

[1] Ifremer, University of Brest, CNRS, IRD, Laboratoire d'Océanographie Physique et Spatiale, Plouzané, France. [2] Department of Meteorology and Bolin Centre for Climate Research, Stockholm University, Stockholm, Sweden. ✉email: damien.desbruyeres@ifremer.fr

The Subpolar North Atlantic (SPNA) plays a fundamental role in the global ocean circulation and therefore in the Earth climate system. It provides a favorable environment for surface waters to mix and sink towards the seafloor before spreading south as part of the Meridional Overturning Circulation (MOC), which transports climate-relevant properties globally (e.g., heat, carbon)[1,2]. It is also the primary gateway for warm and salty Atlantic waters to reach the Nordic Seas and Arctic Ocean[3], and therefore exerts a key control on the mass and heat budgets of those rapidly-changing and most-vulnerable areas[4–6]. Finally, it likely influences atmospheric regimes (e.g., storm tracks) and the development of continental heat waves[7], and could be able to trigger multicentennial climate variability by governing complex processes within the coupled ocean-atmosphere-ice system of the North Atlantic[8].

The climatic imprint of the SPNA is evidently tightly linked to the temperature of its upper layer[9], which is known to respond to both intermittent atmospheric events and decadal-scale changes in ocean circulation and associated heat transport[10–12]. The latter has notably been found responsible for a sudden warming-to-cooling reversal of the SPNA in the mid-2000s[13], with ramifications seen as far as in the sea-level of the East Atlantic shelves and coasts[14]. From an ad hoc observational reconstruction of the meridional heat transport at 45°N derived from the theory of surface-forced water mass transformation, the onset of a new advection-driven reversal in 2016 has been predicted, with suggestive temperature predictions for the early 2020s approaching their previous 2005–2006 maximum[15]. Here, we employ new observational and statistical approaches to document this recent and ongoing warming trend in the context of decadal-scale variability and demonstrate its dominant circulation-driven mechanism, namely the increased poleward transport of warm subtropical water.

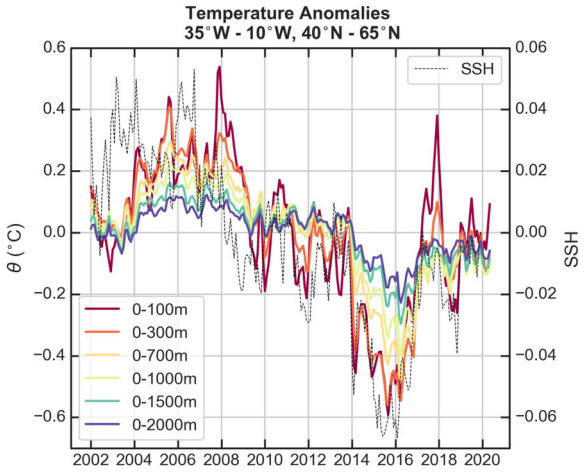


Fig. 1 Temperature and sea-level anomalies in the eastern SPNA. Observed (deseasonalized) temperature anomalies in the eastern SPNA (10°W–35°W, 40°N–65°N) averaged within layers of increasing thickness. The reference period is 2002–2019. The thin dashed line shows anomalies in altimetry-derived sea surface height (global-mean removed) in the eastern SPNA.

Results

Entering a new warming phase. Our analysis targets the broad eastern portion of the SPNA since this is where significant decadal-scale temperature anomalies first transit before spreading cyclonically within the gyre circulation and invading the western portion of the domain[16]. An ocean analysis product covering the period 2002–2019 and primarily built with Argo-derived hydrographic profiles[17] is used to show the evolution of temperature anomalies in the eastern SPNA (10°W–35°W, 40°N–65°N), as averaged above a range of depth levels and relative to the 2002–2019 reference period (Fig. 1). On top of rapid intra-annual changes, the record is dominated by two trend reversals in 2006 and 2016. The former interrupts a decadal warming of the region triggered in the mid-1990's by a surge in the meridional oceanic heat transport at the entrance of the SPNA[18,19]. The following 10 years were marked by a gradual cooling and punctuated by a sharp drop in 2014–2015—the well-documented SPNA cold anomaly partly driven by anomalously strong ocean heat loss to the atmosphere[10]. Since 2016, however, the temperature tendency is seen to have changed sign again suggesting that the SPNA has most likely entered a new warming phase, i.e., the main focus of this study.

The decadal temperature reversal in the SPNA (Fig. 1) is surface-intensified but is still apparent when averaging the temperature of the water column down to 2000 m depth. They have induced concomitant and significant changes in sea surface height (SSH), as illustrated here by a strong agreement on intra-annual to decadal timescales between temperature anomalies and altimetry-derived SSH anomalies (dashed line in Fig. 1; $r = 0.82$ with 0–100 temperature time series). Overall, the ocean heat content (OHC) of the 0–2000 m layer increased by about 8.5×10^{21} J between April 2016 and December 2019, with 80% of this heat gain found above 700 m depth. Anomalous air-sea heat fluxes during this time-span suggests that the recovery from an intermittent period of extreme ocean heat loss in 2014–2015[10] potentially contributed to about a quarter of that value (Supplementary Figure 1). Thus, this leaves ocean heat transport convergence as a dominant contributor, and the remaining of the paper focuses on the dynamical mechanism underlying this specific contribution.

Basin-scale warming and shifting currents. The horizontal pattern of upper (0–100 m) temperature changes in the northern North Atlantic from the cold 2014–2016 period to the warm 2017–2019 period shows a large area of positive anomalies with a maximum magnitude of 0.6 °C and covering the Iceland Basin, the Iberian plain, and the eastern Newfoundland basin (Fig. 2a). The concomitant distribution of air-sea heat flux anomalies confirms their minor (yet non-negligible) contribution to the warming trend (Supplementary Figure 1). As expected, the distribution of SSH anomalies shows a consistent pattern (Fig. 2b), with positive anomalies covering most of the eastern SPNA, which is where the largest thermosteric contributions to SSH changes are known to occur[20]. Those recent SSH changes are particularly intense in the Iceland Basin where the northern and strongest branch of the North Atlantic Current (NAC)—the subpolar front—is observed[21] (see Fig. 2d for a schematic of the circulation features relevant to the present study).

This particular SSH distribution and the strong correlation between upper temperature and SSH tend to support the advective origin of the warming, and a first glimpse into concomitant changes in the intensity and pathway of surface currents is provided by the mean kinetic energy (MKE) calculated from the altimetry-derived geostrophic velocity field (Fig. 2c). A striking intensification of the subtropical portion of the NAC, also visible as an increased SSH cross-stream gradient (Fig. 2b), is observed south of 45°N and west of 30°W. The large MKE positive anomalies in the western subtropics can be tracked downstream within the northern branch of the NAC (circa 50°N), while negative anomalies occupy its southern portion. This overall MKE pattern is in good agreement with Lagrangian model experiments showing that stronger subtropical inflows within the

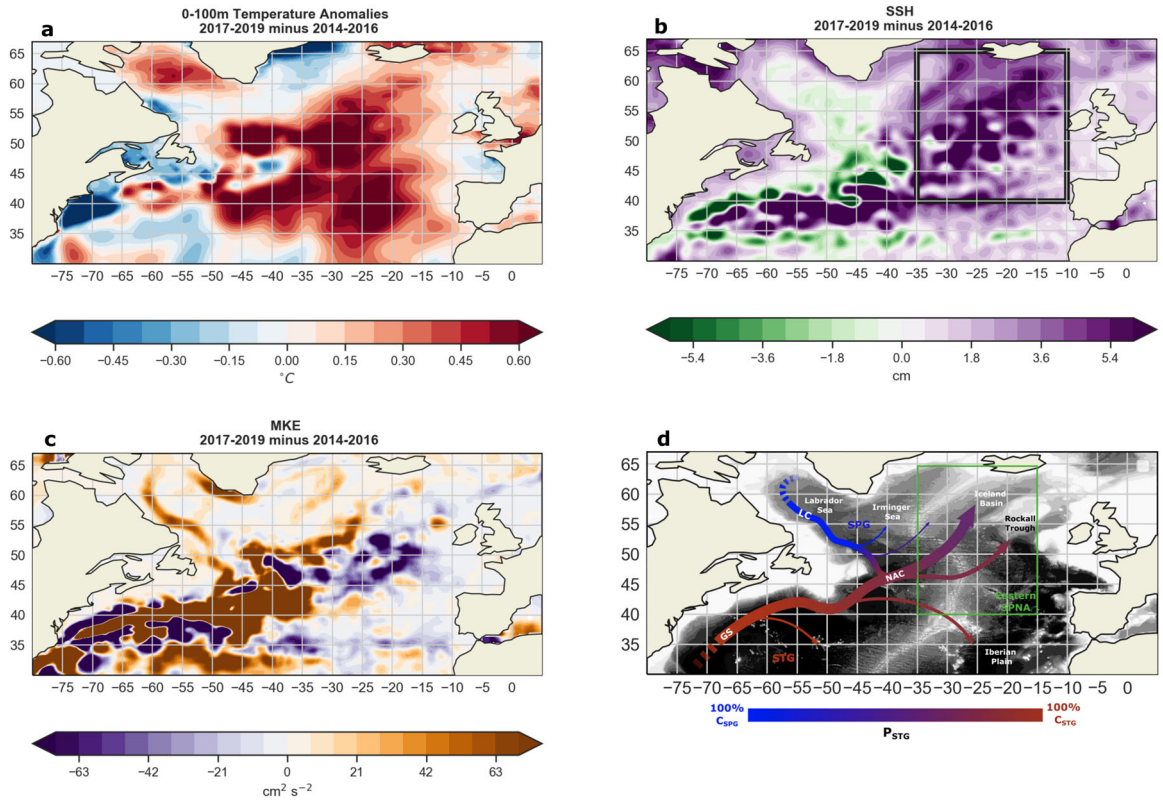


Fig. 2 Spatial patterns of recent changes. a Horizontal pattern of observed temperature anomalies in the upper 0–100 m layer computed as 2017–2019 minus 2014–2016. **b**, **c** Same as (**a**) but for altimetry-derived SSH and MKE, respectively. The black box in (**b**) shows the eastern SPNA region considered in Fig. 1. **d** shows a schematic of the northern North Atlantic circulation with features relevant to the present study highlighted. The Labrador Current (LC) of the Subpolar Gyre (SPG) and the Gulf Stream (GS) of the Subtropical Gyre (STG) connect near Flemish Cap within the North Atlantic Current (NAC) that feeds the eastern SPNA with a mixture of cold subpolar waters (blue - C_{SPG}) and warm subtropical waters (red, C_{STG}). The relative proportion of these two source waters, denoted P_{STG} in the present study and represented by the color scale here, is the key quantity behind temperature trend reversals in the eastern SPNA (green box as considered here).

NAC drive an increased (decreased) transport of its northern (southern) branch in the eastern SPNA[22]. This observed seesaw of the NAC branches in the eastern SPNA is often described as "contraction" and "expansion" of the subpolar gyre (SPG) and subtropical gyre (STG). The associated changes in the relative proportion of warm waters (i.e., from the western subtropical gyre) and cold waters (i.e., from the western subpolar gyre) in the eastern SPNA are likely to drive significant temperature changes[19,23–25] (see Fig. 2d for a schematic of the source water pathways feeding the eastern SPNA).

Passive tracing of advective origins. To evidence and quantify the potential link between the observed shift in circulation and the 2016-to-present warming of the SPNA, we first turn to a simple advection-diffusion model for a passive tracer of local concentration C:

$$\frac{\partial C}{\partial t} = -\langle \mathbf{v} \rangle \cdot \nabla C + \kappa \cdot \nabla^2 C \qquad (1)$$

This simple model enables to extract from surface Eulerian velocities and mesoscale eddy diffusivities a Lagrangian decomposition of the eastern SPNA water mass origins (see schematic in Fig. 2d). Two separate experiments are conducted, in which tracers are kept constant (i.e., $C = 1$) in either a western subtropical box (Fig. 3a) or a western subpolar box (Fig. 3b). They are allowed to evolve freely from those source regions for N years within a N-year mean altimetry-derived surface geostrophic current field v and a background surface eddy field parametrized with an observation-based estimate of mesoscale eddy diffusivities κ[26]. We will refer to the final tracer concentration in these two experiments as C_{STG} and C_{SPG}, respectively. The experiments are run for successive and overlapping N-year windows so that the final distribution of C associated with year y is the result of N years of tracer advection within the altimetry-derived velocity field $\langle \mathbf{v} \rangle = \frac{1}{N} \int_{t=y-N+1}^{t=y} \mathbf{v} dt$. Dependency to the parameter N, which represents a typical advective timescale of surface waters between the two source regions and the eastern SPNA, is evaluated through an ensemble mean and an ensemble spread (standard deviations) of model outputs with $N = 2$, 3, and 4 years (Methods and Supplementary Fig. 4). The choice of N was guided by the literature[27,28] and validated herein via an additional tracer experiment that quantified the mean travel-time of tracers between the two source regions and the eastern SPNA (Supplementary Fig. 2).

Noteworthy, the non-inclusion of surface Ekman velocities—which should, in reality, hamper the surface exchange of C_{STG} across the inter-gyre boundary[27,29,30]—enables the tracers to be strictly advected within a velocity field that primarily reflects the surface-intensified first baroclinic mode and the motions of the main thermocline[31]. The altimetry-derived geostrophic surface circulation used herein is hence likely to be a fair proxy of the large-scale upper circulation and its changing intensity and horizontal structure[32]. The consistency between *geostrophic* surface and interior pathways will be demonstrated herein with

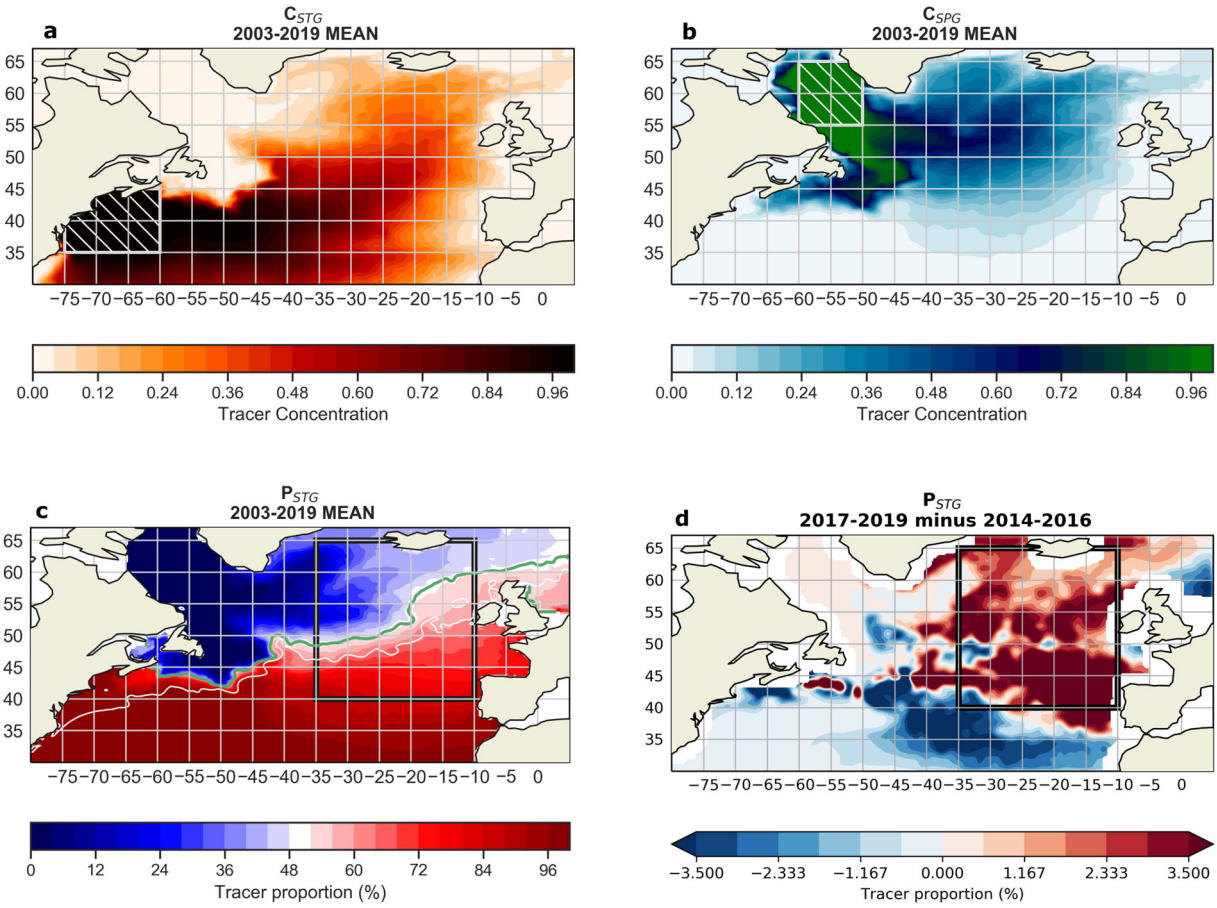


Fig. 3 Spatial distributions of passive tracers. a The time-mean 2003–2019 final distribution of C_{STG} (see text and Methods). **b** Same as (**a**) for C_{SPG}. (**c**). The proportion of subtropical-origin water computed from (**a**) and (**b**) as $P_{STG} = \frac{C_{STG}}{C_{STG}+C_{SPG}}$. The green line shows the 50% isoline of P_{STG} and the white line indicates the zero sea surface height contour. **d** The horizontal pattern of P_{STG} change from 2014–2016 to 2017–2019.

a companion tracer experiment run on the three-dimensional velocity field of an ocean reanalysis (ECCOv4r4[33]), as well as with a statistical clustering of vertical ocean properties.

The long-term mean (2003–2019) final distributions of C_{STG} and C_{SPG} show the general pathways of the two main source waters composing the inter-gyre flow (Fig. 3a, b). From those, the local proportion of western-origin subtropical water $P_{\mathrm{STG}} = \frac{C_{\mathrm{STG}}}{C_{\mathrm{STG}}+C_{\mathrm{SPG}}}$ (and western-origin subpolar water $P_{\mathrm{SPG}} = 1 - P_{\mathrm{STG}}$) can be deduced (Fig. 3c). The Lagrangian nature of P_{STG} provides an alternative view of circulation contours and gyre shapes usually derived directly from SSH patterns[34,35]. More importantly, it here enables a direct link with the pathways and upstream properties of both source waters advected by the NAC along the intergyre boundary. The time-mean proportion of subtropical-origin and subpolar-origin surface waters in the eastern SPNA box amounts to 60% and 40%, respectively (in line with Lagrangian decomposition of the eastern SPNA thermocline waters in a hindcast simulation[22]). We note here that the contribution of parametrized eddy mixing to the distributions of C_{STG} and C_{SPG} is as expected substantially smaller than the advective contribution and has the average effect of decreasing P_{STG} in the eastern SPNA box by about 4% (Supplementary Fig. 3).

Running the Lagrangian experiment with successive (and overlapping) N-year averaged velocities enables to construct a time series of P_{STG} within the eastern SPNA and to compare it with a time series of temperature anomalies of the upper layer (Fig. 4a). The striking correlation between those two quantities, with the variability of P_{STG} capturing both trend reversals circa 2006 and 2016, suggests a clear causal relationship (estimated here as 0.05 °C/%). The respective evolutions of C_{STG} and C_{SPG} reveal the important role of the former in driving P_{STG} variability, and most particularly in driving the latest and abrupt cooling-to-warming reversal. There is likewise a good agreement between the horizontal patterns of temperature and P_{STG} increase (Fig. 2a and Fig. 3d, respectively), with positive anomalies covering most of the eastern SPNA. Negative P_{STG} anomalies in the central and eastern subtropics further highlight the recent enhanced penetration of warm subtropical waters[36], which, in turn, agrees with the observed intensification of the northern NAC branch (Fig. 2c). We also note a consistent northward displacement of the 50% P_{STG} isoline—an indicative measure of the gyre expansions and contractions—from its 2015 southernmost position, with the C_{STG}-dominated region currently expanding into the Iceland Basin (Supplementary Fig. 5). Overall, all important changes revealed by the simple model are, as expected, associated with horizontal advection[11,19,24,25,37] (thin lines in Fig. 4a; note that because κ is time-invariant, the time-varying diffusive signal reflects changes in large-scale advective pathways only).

Following our previous discussion on the representativeness and use of surface (geostrophic) velocities to diagnose changes in interior pathways, we evaluate a companion experiment performed with the three-dimensional velocity field of the

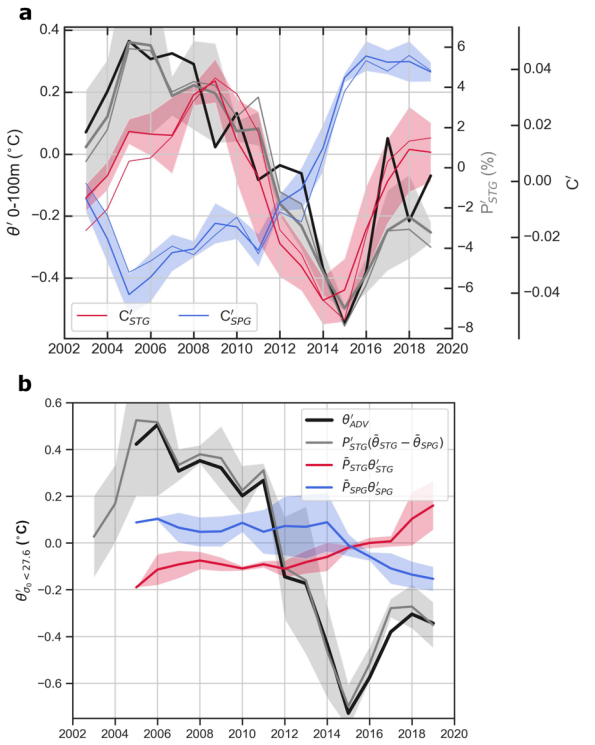


Fig. 4 Advective origin of temperature variability in the eastern SPNA. **a** Comparison of observed 0–100 m temperature anomalies annually averaged in the eastern SPNA (black line) with observed anomalies in the proportion of subtropical-origin water P'_{STG} in the same region (gray line) and the anomalous concentrations C'_{STG} (red) and C'_{SPG} (blue). Thin lines show the advective contribution. Shadings are ±1 standard deviation. See Eq. 1 and Methods for details. **b** Reconstruction of advection-driven temperature anomalies in the eastern SPNA for σ_0 < 27.6 kg m^{-3} as the sum of three distinct contributions: anomalies in the relative proportion of subtropical-origin water (gray), anomalies in the initial temperature of subtropical-origin water (red), and anomalies in the initial temperature of subpolar-origin water (blue). Shadings are ±1 standard deviation. See Eq. 2 and Methods for details.

ECCOv4r4 ocean state estimate[33]. An identical model setup (with the advective scheme augmented by a vertical component) is used to infer the mean and anomalous concentration of C_{STG} and C_{SPG} from the surface to about 700 m depth (recall that decadal temperature signal we focus on is largely contained above 700 m depth). Our purpose here is strictly to demonstrate that the large-scale geostrophic pathways are largely coherent from the surface down to the main pycnocline, using an ocean model that should best reconcile the surface altimetry fields with interior observational constraints—i.e., we do not intend to reproduce dedicated model-based analysis of those pathways, which are published elsewhere, and for which higher-resolution simulations could be preferred. We first note that the time-mean horizontal distributions of C_{STG} and C_{SPG} appear similar to the altimetry-derived fields but also highlight some discrepancies associated with well-known deficiencies of low-resolution numerical models in the region (e.g., note the absence of a proper Northwest Corner at the intergyre boundary, Supplementary Fig. 6). In line with aforementioned works, the northward penetration of C_{STG} is maximum below the Ekman layer (peaking at 100 m), while the eastward penetration of subpolar tracer is surface-intensified (i.e., Ekman drift is enhancing the eastward tracer advection from the Labrador Sea). Most importantly, the (decadal) changes in C_{STG} and C_{SPG} are vertically-coherent between the base of the Ekman layer and the depth of the main pycnocline (taken here to be σ_0 = 27.6), i.e., within the natural layer along which tracers can efficiently spread and mix from both source regions (Supplementary Fig. 6). Because geostrophic currents are not likely to significantly change from the surface to the base of the Ekman layer, we conclude that altimetry-derived surface flows allow to capture large-scale changes in the interior circulation (in line with ref. [31]) and in the associated propagation of the two primary water masses that compose the upper layer of the eastern SPNA.

To better quantify the relative importance of P_{STG} (or P_{SPG}) changes in driving the observed temperature signal in the eastern SPNA, we now associate those changes with the initial temperature of both source waters θ_{STG} and θ_{SPG} as averaged within their respective source regions (boxes in Fig. 3a, b) using the following equation:

$$\theta'_{ADV} = P'_{STG}\left(\overline{\theta_{STG}} - \overline{\theta_{SPG}}\right) + \overline{P_{STG}}\theta'_{STG} + \overline{P_{SPG}}\theta'_{SPG} \quad (2)$$

This reconstruction enables to decompose the advection-driven temperature anomalies θ'_{ADV} of the eastern SPNA into three distinct contributions and to evaluate their relative importance for the heat budget of the region. In line with the tracer experiment configuration, we assume a typical timescale of N years for temperature anomalies to be advected adiabatically above the main pycnocline (σ_0< 27.6) from their source regions to the eastern SPNA where they mix into a single water mass (see Methods). Three distinct drivers of temperature variability are thereby considered: anomalies in the relative proportion of the source waters (first term in r.h.s. of Eq. 2) and anomalies in their respective initial temperature (second and third terms). It is found that the first of these contributions largely dominates the others, confirming that shifts in the large-scale circulation projecting onto the time-mean ocean thermal structure is the primary mechanism triggering basin-scale reversals of temperature trends in the SPNA (Fig. 4b). The advection of remote temperature anomalies from both source regions remain non-negligible and consistently tend to oppose themselves—most especially since 2013—in line with the well-known dipole pattern of temperature anomalies between the western subtropical and subpolar regions[38–40].

Statistical clustering of water masses. An alternative confirmation of the importance of circulation shifts in driving the recent cooling-to-warming reversal in the eastern SPNA is provided by applying a machine learning algorithm—namely a profile classification model (PCM)—to our three-dimensional observational dataset[41]. The PCM is built upon a synthetic statistical and unsupervised classification of ocean vertical profiles into a chosen number of "clusters" or "classes" using the classical "Gaussian Mixture Model" method. Once trained, the PCM can be used to assign any given profile to its most probable class (see Methods). It is herein used to reveal coherent temporal and spatial patterns in the SPNA and to further verify whether the altimetry-derived results (i.e., surface-focused advective shifts) are representative of the ocean interior. In other words, we seek to complement the Lagrangian clustering of surface pathways with a statistical clustering of interior ocean properties, which in the present case is an indirect indicator of anomalous three-dimensional pathways (i.e., anomalous penetration of stratified subtropical waters into the vertically-homogeneous subpolar gyre).

As pointed out repeatedly in PCM analysis[41–43], the determination of the most appropriate number of clusters can only be indicatively given by statistical metrics (e.g., Bayesian Information Criteria[44]) and it is the scientific meaning of the clusters for the given purpose that must prevail. Because our present goal is to mimic the altimetry-based and objectively distinguish the typical

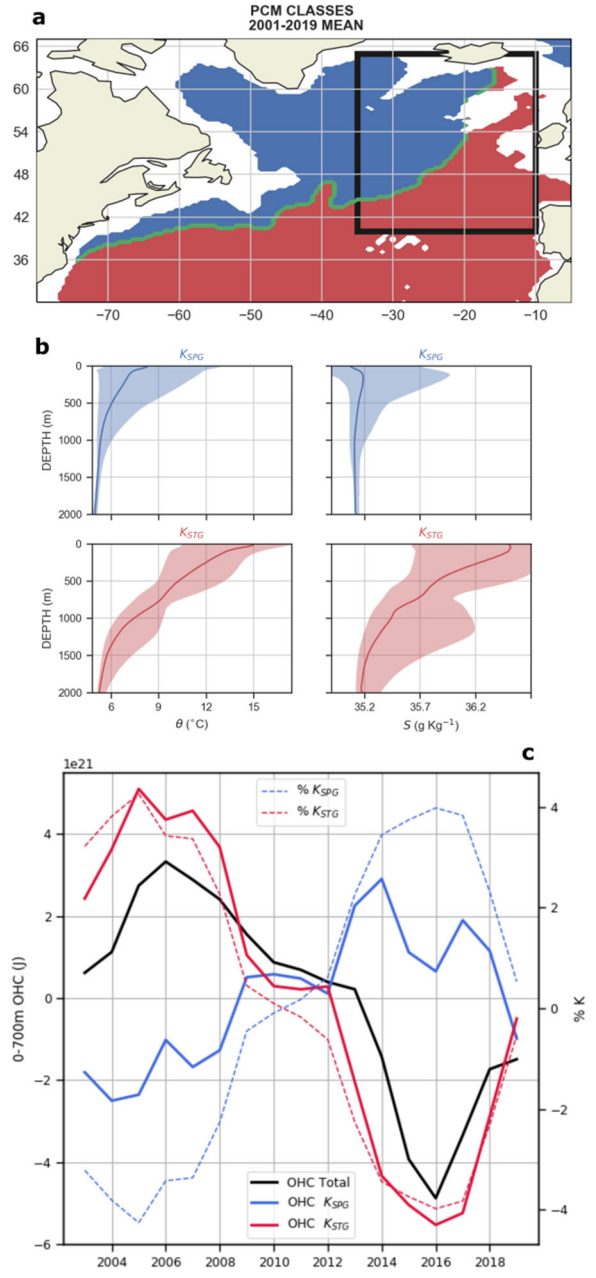


Fig. 5 Clustering of eastern SPNA water masses. a The horizontal distribution of the two classes K_{STG} (red) and K_{SPG} (blue) obtained from the long-term mean (2001–2019) temperature and salinity fields, and **b** their respective temperature and salinity vertical structures. Profiles where depth does not exceed 2000 m (white shadings) were not included in the PCM. **c** The OHC anomalies relative to the 2003–2019 period of the upper 0–700 m layer of the eastern SPNA (black box, black line) decomposed into contributions from K_{SPG} (solid blue) and K_{STG} (solid red). Anomalies in the box-averaged proportion of those two classes are shown with dashed lines.

vertical structures of (homogeneous) subpolar and (stratified) subtropical water masses, we employ a simple approach and train a 2-class PCM using the 2002–2019 temperature and salinity gridded product (see Methods). The reader is referred to Supplementary Fig. 7 for the presentation of a 3-class PCM.

The horizontal distribution of the subpolar and subtropical classes, referred to as K_{STG} and K_{SPG} hereafter, is shown in Fig. 5a along with their respective temperature and salinity vertical structures and associated spread in Fig. 5b. One will easily note the close resemblance with the altimetry-derived distribution of P_{STG} previously obtained (Fig. 3c). Here, the PCM provides the missing information on the typical vertical structure of both "water masses", with subpolar waters being logically colder, fresher, and less stratified than their subtropical neighbors. This trained PCM is finally used to classify each year of the data set and to reveal the role of both classes in explaining the observed temperature variability. This role is quantified by computing the respective contribution of each class K to the total OHC of the 0–700 m eastern SPNA as:

$$OHC_K(t) = \iint_{x,y} p_K(x,y,t)\left[\int_{z=700m}^{0} \rho_0 C_p \theta(x,y,z,t)dz\right]dxdy \quad (3)$$

with p_K being the time-varying local probability that a given θ profile belongs to the considered class K (i.e., K_{STG} or K_{SPG})[45]. The resulting time series concur with the tracer-based monitoring of P_{STG}: since the mid-2000s and until the mid 2010s, in the eastern SPNA the relative proportion of K_{STG} decreased and the proportion of K_{SPG} increased, so did their associated OHC contributions (Fig. 5c). From the mid-2010s, trends reversed and K_{STG} and K_{SPG} respectively started to increase and decrease their OHC contributions. One will note that this recent decrease in OHC_{KSPG} seemingly preceded that of K_{SPG} proportion, which is in line with the local atmospheric drivers (air-sea heat fluxes) of the subpolar cold anomaly that occurred during 2014–2015. Because of their different mean background temperature profile (Fig. 5b), OHC_{KSTG} overcomes OHC_{KSPG} overall and accounts for both trend reversals in 2006 and 2016. Therefore, both surface-based index (Fig. 3) and stratification-based index (Fig. 5) of source water pathways concur with one another in pointing out a significant circulation shift and increased penetration of warm subtropical waters into the eastern SPNA since 2016.

Conclusion and discussion

This study documents an ongoing large-scale hydrographic change occurring within the upper layer of the SPNA: the decade-long cooling trend prevailing since 2006 rapidly reversed in 2016 and a large-scale warming settled in the central and eastern portions of the domain. The responsible mechanism—also at play for the previous warming-to-cooling reversal in 2006—was revealed with observational datasets by solving a simple altimetry-based advective model for a passive tracer and by performing a statistical clustering of ocean in situ profiles.

This combined approach provided two independent and observation-based decompositions of eastern SPNA waters into subtropical-origin and subpolar-origin waters, and both depicted the changing relative proportion of these two source waters as a predominant cause for the 2016 trend reversal. Confirming previous model-based analyses of the eastern SPNA heat budget[19,25,46], this change was more specifically induced by a rapid increase in the northeastward transport of warm subtropical waters within the North Atlantic Current, in line with a concomitant strengthening of the MOC heat transport as detected across 45°N[15] and presumably pending at 26°N[47].

Embedded within the large-scale cyclonic gyre circulation, this warming signal is expected to spread westward from its current eastern SPNA location and progressively invade the Irminger and Labrador Sea while propagating to greater depth via boundary-focused mixing and sinking[48]. This warming signal may also influence the intensity of light-to-dense water mass transformation and the depth of open-ocean convective mixing in those regions, and hence the forthcoming magnitude of the Atlantic MOC and related property transports. Ongoing investigations are specifically dedicated to this important issue.

The variability of the SPNA heat content is known to exert a key influence on the so-called Atlantic Multidecadal Variability (AMV)—index based on sea surface temperature—that is generally used to characterize the climate of the North Atlantic and its global-scale ramifications[49–52]. In fact, it was recently suggested that the AMV would soon transition towards a negative (i.e., cold) phase owing to the cooling of the SPNA since the mid-2000s[53]. It is too early to ascertain the low-frequency nature of the ongoing SPNA warming described herein, and whether this thermal reversal will ultimately damp the current downturn of the AMO index remains as of now an open question[54] (see Supplementary Fig. 8 for an updated AMV index). We argue, however, that the advective origin of the ongoing SPNA warming and the long ocean memory of this region[55] makes it likely to persist over the coming years. Several indicators in fact describe oceanic and atmospheric conditions similar to those of the mid-1990's when another sharp cooling-to-warming reversal triggered a decade-long warming trend[18]. Those indicators include the preceding persistence of strongly positive North Atlantic Oscillation conditions (see Supplementary Fig. 8), the occurrence of relatively deep convective activity[56,57] and intense water mass transformation in the SPNA in the preceding winters[28], and a resulting intensification of the MOC and its meridional heat transport across the southern SPNA boundary[15]. Investigating and separating the atmospheric drivers of the ocean-focused changes and mechanisms reported herein will motivate a follow-up study.

Methods

ISAS-15 temperature and salinity gridded fields. The observational in situ dataset used is the In Situ Analysis System, which provides gridded three-dimensional fields of temperature and salinity during 2002–2019[58]. Originally based on the Argo network of profiling floats, ISAS is now optimally interpolating all types of vertical profile (e.g., XBTs, CTDs) and time series. The version used here is ISAS15 and is available online[17]. Data were quality-controlled in delayed mode for the years 2002–2016 and in near-real-time mode for 2017–2019, with this difference in data treatment having no impacts on the large-scale temperature anomalies investigated herein. The field of eddy diffusivities was computed by[26] from observational data and theory and is available online at https://figshare.com/articles/Groeskamp_et_al_2020_-_mixing_diffusivities/12554555.

Satellite altimetry. The dataset for the sea surface height (SSH) and associated geostrophic velocities used to derive the mean kinetic energy (MKE) is the DUACS DT2018 multimission satellite altimetry[59]. The data is on a 1/4° grid resolution and spans the period from January 1993 until December 2019. Since the delayed time data is only available until May 2019, we extended the data until December 2019 using with the near-real-time fields.

NCEP atmospheric fluxes. The atmospheric fluxes used here are derived from the 1948 to 2019 NCEP/NCAR reanalysis[60]. The net heat flux was derived by adding the shortwave, longwave, sensible and latent heat flux. For the momentum fluxes, we used the zonal and meridional wind stress to derive the wind-stress curl. The horizontal grid resolution of the data is 2.5° × 2.5°.

ECCOv4r4 ocean state estimate. The state-of-the-art ocean state estimates Estimating the Circulation and Climate of the Ocean (ECCO) are based on least-squares fitting of the Massachusetts Institute of Technology General Circulation Model to numerous types of global-scale ocean observations during 1992–2017. ECCO is thoroughly described in the literature[33] and was shown to be a good fit to observations of global-scale and basin-scale ocean heat content, especially in analysis of the North Atlantic heat budget[11,48]. We here use the monthly interpolated field of the ECCOv4 Release 4, which were downloaded from https://ecco.jpl.nasa.gov/drive/files/Version4/Release4.

NAO index. The NAO index data was provided by the Climate Analysis Section, NCAR, Boulder, USA, Hurrell (2003). Hurrell, James & National Center for Atmospheric Research Staff (Eds). Last modified 24 Apr 2020. "The Climate Data Guide: Hurrell North Atlantic Oscillation (NAO) Index (station-based)." Retrieved from https://climatedataguide.ucar.edu/climate-data/hurrell-north-atlantic-oscillation-nao-index-station-based. Accessed on 01 July 2020.

Tracer advection and diffusion model. Equation 1 is solved on a subset of the ¼° cartesian AVISO grid using a forward timestep and an upstream differencing scheme for the advective terms. An explicit 2-time level scheme is used with a timestep of 1500 s. The open boundary conditions for the overall domain are set as $\frac{\partial C}{\partial x} = 0$ and $\frac{\partial C}{\partial y} = 0$. The diffusive term is built upon a recent estimate of the three-dimensional mesoscale eddy diffusivities from observation data and theory[26]. Two types of experiments are conducted in which the initial tracer concentration is set to C=0 everywhere except in a western subtropical box ($C_{STG} = 1$; 60°W–75°W, 35°N–45°N) or a western subpolar box ($C_{SPG} = 1$; 50°W – 60°W, 55°N – 65°N). We note that the present definitions of the subtropical and subpolar boxes encompass the bulk of the western boundary currents of both gyres (i.e., the Gulf Stream and the West Greenland and Labrador Currents, respectively) that connect with each other as the North Atlantic current downstream near Flemish Cap and the Grand Banks of Newfoundland. In the case of the subtropical box, we hence consider the Northern Recirculation Gyre[61] as part of the subtropical source region. The tracer is then allowed to spread freely during N years within a N-year mean surface geostrophic velocity fields obtained from altimetry data while being kept constant within the source regions. The experiments are run for successive and overlapping N-year windows so that the final distribution C associated with year y is the result of N years of tracer advection within the velocity field $\langle \mathbf{v} \rangle = \frac{1}{N} \int_{t=y-N+1}^{t=y} \mathbf{v} dt$. In order to ensure the robustness of the method, the time series presented in the paper are ensemble mean of three experiments using different (yet realistic) typical surface advective time scales $N = 2$, $N = 3$, and $N = 4$ years. Those values were deduced from a separate tracer experiment in which tracer was added once in the western STG and western SPG boxes and advected freely froward during 10 years within the time-mean (2002-2019) velocity field. The tracer concentration was averaged within the eastern SPNA box at each time step of the model integration, providing a precise quantification of the advective timescale from both region (Supplementary Fig. 2). The spread (i.e., standard deviation) between the results of the experiment is used as an uncertainty range in Fig. 4 (see Supplementary Fig. 4 for the individual time series from these experiments). An identical model setup was used in the ECCOv4r4 tracer experiment, with the vertical component of advection added to the advective scheme, and the tracer concentration set to unity over the full vertical extent of the source regions ($C_{STG} = 1$; 60°W–75°W, 35°N–45°N, surface-bottom) or a western subpolar box ($C_{SPG} = 1$; 50°W–60°W, 55°N–65°N, surface-bottom). Final tracer concentrations were eventually averaged above the main pycnocline, taken here to $\sigma_0 = 27.6$ kg m^{-3}.

The local proportion of western-origin subtropical water $P_{\mathrm{STG}} = \frac{C_{\mathrm{STG}}}{C_{\mathrm{STG}} + C_{\mathrm{SPG}}}$ (or equivalently western-origin subpolar water $P_{\mathrm{SPG}} = 1 - P_{\mathrm{STG}}$) in the SPNA is then calculated. It is used to estimate the three primary advective drivers of temperature changes in the eastern SPNA using Eq. 2. $\overline{\theta_{\mathrm{STG}}}$ and $\overline{\theta_{\mathrm{SPG}}}$ represent the time-mean initial temperature of subtropical and subpolar source waters as averaged above $\sigma_0 = 27.6$ kg m^{-3}. This isopycnal is chosen here to represent the main pycnocline of the domain above which the two source waters spread downstream (several tests were performed with σ_0 ranging between 27.1 and 27.7 and limited impacts on the results were found). θ'_{STG} and θ'_{STG} represent departure from $\overline{\theta_{\mathrm{STG}}}$ and $\overline{\theta_{SPG}}$. Their respective time series are out-phased by N years in Eq. 2 to account for the appropriate advection timescales of anomalies from their source regions to the eastern SPNA.

Profile classification model. A PCM with $K = 2$ classes was trained on vertical temperature and salinity profiles from 2002 to 2019 time mean of the ISAS dataset (described above). Only profiles where depth does exceed 2000 m were included in the PCM. Each variable was first normalized by vertical levels (e.g., all-temperature values at 200 m are centered and standardized, this allows for deep structures to be preserved against the more diverse surface values) and secondly compressed using a principal component analysis (to reduce the number of vertical dimensions to a few eigen values). Then a Gaussian Mixture Model with 2 modes is fitted on reduced profiles using a classic Expectation-Maximization algorithm[62] (See[41] for full details of the PCM methodology and[43] for the presentation of a PCM with two variables). Finally, temperature and salinity profiles of the full ISAS15 time series are classified using the fitted PCM, i.e., the p_K posterior probabilities of the Gaussian Mixture components (clusters) are computed at each grid points. A PCM is a fuzzy classifier because the p_K can vary from 0 to 1 and their sum for each profile is 1. This means that each grid point is classified and can possibly be in a smooth intermediate position between the cluster core structure. This also means that the grid cell heat content is preserved if split into each cluster (see Eq. 3). It is important to note that the PCM training does not consider the latitude/longitude of profiles. Therefore, the cluster distribution in space naturally arises from similarities and coherence in ocean interior structures. To compute the typical vertical structures of clusters, we used the mean and standard deviation of profiles attributed to a given class. The PCM analysis was conducted using the *pyXpcm* software[63].

Data availability

The datasets generated during and/or analyzed during the current study are available from the corresponding author on reasonable request.

Code availability

The codes that support the findings of this study are available from the corresponding author upon reasonable request.

Received: 21 August 2020; Accepted: 1 February 2021;
Published online: 26 February 2021

References

1. Wunsch, C. What is the thermohaline circulation? *Science* **298**, 1179–1181 (2002).
2. Buckley, M. W. & Marshall, J. Observations, inferences, and mechanisms of the Atlantic Meridional Overturning Circulation: a review. *Rev. Geophys.* **54**, 5–63 (2016).
3. Chafik, L. & Rossby, T. Volume, heat, and freshwater divergences in the Subpolar North Atlantic suggest the Nordic Seas as key to the state of the Meridional Overturning Circulation. *Geophys. Res. Lett.* 4799–4808 (2019), https://doi.org/10.1029/2019GL082110.
4. Wang, Q. et al. Intensification of the Atlantic water supply to the Arctic Ocean through Fram strait induced by Arctic Sea Ice decline. *Geophys. Res. Lett.* **47**, e2019GL086682 (2020).
5. Holliday, N. P. et al. Reversal of the 1960s to 1990s freshening trend in the northeast North Atlantic and Nordic Seas. *Geophys. Res. Lett.* **35**, 1–5 (2008).
6. Langehaug, H. R., Medhaug, I., Eldevik, T. & Otterå, O. H. Arctic/Atlantic exchanges via the subpolar gyre*. *J. Clim.* **25**, 2421–2439 (2012).
7. Duchez, A. et al. Drivers of exceptionally cold North Atlantic Ocean temperatures and their link to the 2015 European heat wave. *Environ. Res. Lett.* **11**, 074004 (2016).
8. Moreno-Chamarro, E., Zanchettin, D., Lohmann, K. & Jungclaus, J. H. An abrupt weakening of the subpolar gyre as trigger of Little Ice Age-type episodes. *Clim. Dyn.* **48**, 727–744 (2017).
9. Chafik, L. et al. Global linkages originating from decadal oceanic variability in the subpolar North Atlantic. *Geophys. Res. Lett.* **43**, 10,909–910,919 (2016).
10. Josey, S. A. et al. The recent Atlantic cold anomaly: causes, consequences, and related phenomena. *Ann. Rev. Mar. Sci.* **10**, 475–501 (2018).
11. Piecuch, C. G., Ponte, R. M., Little, C. M., Buckley, M. W. & Fukumori, I. Mechanisms underlying recent decadal changes in subpolar North Atlantic Ocean heat content. *J. Geophys. Res. Ocean.* **122**, 1–17 (2017).
12. Häkkinen, S., Rhines, P. B. & Worthen, D. L. Heat content variability in the North Atlantic Ocean in ocean reanalyses. *Geophys. Res. Lett.* **42**, 2901–2909 (2015).
13. Robson, J., Ortega, P. & Sutton, R. A reversal of climatic trends in the North Atlantic since 2005. *Nat. Geosci.* **9**, 513–517 (2016).
14. Chafik, L., Nilsen, J. E. Ø., Dangendorf, S., Reverdin, G. & Frederikse, T. North Atlantic Ocean Circulation and Decadal Sea level change during the Altimetry Era. *Sci. Rep.* **9**, 1–9 (2019).
15. Desbruyères, D. G., Mercier, H., Maze, G. & Daniault, N. Surface predictor of overturning circulation and heat content change in the subpolar North Atlantic. *Ocean Sci* **15**, 809–817 (2019).
16. Kwon, Y. O. & Frankignoul, C. Mechanisms of multidecadal atlantic meridional overturning circulation variability diagnosed in depth versus density space. *J. Clim.* **27**, 9359–9376 (2014).
17. Nicolas Kolodziejczyk, Prigent-Mazella, A. & Fabienne Gaillard. ISAS-15 temperature and salinity gridded fields. (2017), https://doi.org/10.17882/52367.
18. Robson, J., Lohmann, K., Smith, D. & Palmer, M. D. Causes of the rapid warming of the North Atlantic Ocean in the mid-1990s. *J. Clim.* **25**, 4116–4134 (2012).
19. Desbruyères, D., Mercier, H. & Thierry, V. On the mechanisms behind decadal heat content changes in the eastern subpolar gyre. *Prog. Oceanogr.* **132**, 262–272 (2015).
20. Zhang, W. & Yan, X.-H. The subpolar North Atlantic ocean heat content variability and its decomposition. *Sci. Rep.* **7**, 13748 (2017).
21. Lherminier, P. et al. The Atlantic Meridional Overturning Circulation and the subpolar gyre observed at the A25-OVIDE section in June 2002 and 2004. *Deep. Res. Part I Oceanogr. Res. Pap.* **57**, 1374–1391 (2010).
22. Desbruyères, D., Thierry, V. & Mercier, H. Simulated decadal variability of the meridional overturning circulation across the A25-Ovide section. *J. Geophys. Res. Ocean.* **118**, 462–475 (2013).
23. Häkkinen, S., Rhines, P. B. & Worthen, D. L. Warm and saline events embedded in the meridional circulation of the northern North Atlantic. *J. Geophys. Res. Ocean.* **116**, 1–13 (2011).
24. Hakkinen, S. & Rhines, P. B. Shifting surface currents in the northern North Atlantic Ocean. *J. Geophys. Res.* **114**, 1–12 (2009).
25. Burkholder, K. C. & Lozier, M. S. Tracing the pathways of the upper limb of the North Atlantic Meridional Overturning Circulation. *Geophys. Res. Lett.* **41**, 4254–4260 (2014).
26. Groeskamp, S., LaCasce, J. H., McDougall, T. J. & Rogé, M. Full-depth global estimates of ocean mesoscale Eddy mixing from observations and theory. *Geophys. Res. Lett.* **47**, 1–12 (2020).
27. Brambilla, E. & Talley, L. D. Surface drifter exchange between the North Atlantic subtropical and subpolar gyres. *J. Geophys. Res. Ocean.* **111**, 1–16 (2006).
28. de Boisséson, E., Thierry, V., Mercier, H., Caniaux, G. & Desbruyères, D. Origin, formation and variability of the Subpolar Mode Water located over the Reykjanes Ridge. *J. Geophys. Res. Ocean.* **117**, n/a–n/a (2012).
29. Foukal, N. P. & Lozier, M. S. No inter-gyre pathway for sea-surface temperature anomalies in the North Atlantic. *Nat. Commun.* **7**, 1–6 (2016).
30. Burkholder, K. C. & Lozier, M. S. Subtropical to subpolar pathways in the North Atlantic: deductions from Lagrangian trajectories. *J. Geophys. Res. Ocean.* **116**, 1–12 (2011).
31. Wunsch, C. The vertical partition of oceanic horizontal kinetic energy. *J. Phys. Oceanogr.* **27**, 1770–1794 (1997).
32. Hakkinen, S. Decline of Subpolar North Atlantic Circulation During the 1990s. *Science.* **304**, 555–559 (2004).
33. Forget, G. et al. ECCO version 4: an integrated framework for non-linear inverse modeling and global ocean state estimation. *Geosci. Model Dev.* **8**, 3071–3104 (2015).
34. Foukal, N. P. & Lozier, M. S. Assessing variability in the size and strength of the North Atlantic subpolar gyre. *J. Geophys. Res. Ocean.* 6295–6308 (2017), https://doi.org/10.1002/2017JC012798.
35. Hátún, H. & Chafik, L. On the Recent Ambiguity of the North Atlantic Subpolar Gyre Index. *J. Geophys. Res. Ocean.* **123**, 5072–5076 (2018).
36. Stevens, S. W., Johnson, R. J., Maze, G. & Bates, N. R. A recent decline in North Atlantic subtropical mode water formation. *Nat. Clim. Chang.* **10**, 1-1 (2020).
37. Holliday, N. P. et al. Multidecadal variability of potential temperature, salinity, and transport in the eastern subpolar North Atlantic. *J. Geophys. Res. Ocean.* **120**, 1–23 (2015).
38. Lozier, M. S., Roussenov, V., Reed, M. S. C. & Williams, R. G. Opposing decadal changes for the North Atlantic meridional overturning circulation. *Nat. Geosci.* **3**, 728–734 (2010).
39. Lozier, M. S. et al. The spatial pattern and mechanisms of heat-content change in the North Atlantic. *Science* **319**, 800–803 (2008).
40. Williams, R. G., Roussenov, V., Lozier, M. S. & Smith, D. Mechanisms of heat content and thermocline change in the subtropical and subpolar North Atlantic. *J. Clim.* **28**, 9803–9815 (2015).
41. Maze, G. et al. Coherent heat patterns revealed by unsupervised classification of Argo temperature profiles in the North Atlantic Ocean. *Prog. Oceanogr.* **151**, 275–292 (2017).
42. Jones, D. C., Holt, H. J., Meijers, A. J. S. & Shuckburgh, E. Unsupervised clustering of Southern Ocean Argo float temperature profiles. *J. Geophys. Res. Ocean.* **124**, 390–402 (2019).
43. Rosso, I. et al. Water mass and biogeochemical variability in the Kerguelen Sector of the Southern Ocean: a machine learning approach for a mixing hot spot. *J. Geophys. Res. Ocean.* **125**, e2019JC015877 (2020).
44. Schwarz, G. Estimating the dimension of a model. *Ann. Stat.* **6**, 461–464 (1978).
45. Maze, G., Mercier, H. & Cabanes, C. Profile classification models. *Mercator Ocean J.* **55**, 48–56 (2017).
46. Foukal, N. P. & Lozier, M. S. Examining the origins of ocean heat content variability in the eastern North Atlantic subpolar gyre. *Geophys. Res. Lett.* **45**, 275–283 (2018).
47. Moat, B. I. et al. Pending recovery in the strength of the meridional overturning circulation at 26°N. *Ocean Sci. Discuss.* **2020**, 1–22 (2020).
48. Desbruyères, D. G. et al. Importance of boundary processes for heat uptake in the Subpolar North Atlantic. *J. Geophys. Res. Ocean.* **125**, e2020JC016366 (2020).
49. Sutton, R. T. & Dong, B. Atlantic Ocean influence on a shift in European climate in the 1990s. *Nat. Geosci.* **5**, 788–792 (2012).
50. Delworth, T. L. & Mann, M. E. Observed and simulated multidecadal variability in the Northern Hemisphere. *Clim. Dyn.* **16**, 661–676 (2000).
51. McCarthy, G. D., Haigh, I. D., Hirschi, J. J.-M., Grist, J. P. & Smeed, D. A. Ocean impact on decadal Atlantic climate variability revealed by sea-level observations. *Nature* **521**, 508–510 (2015).
52. Enfield, D. B., Mestas-Nuñez, A. M. & Trimble, P. J. The Atlantic Multidecadal Oscillation and its relation to rainfall and river flows in the continental U.S. *Geophys. Res. Lett.* **28**, 2077–2080 (2001).
53. Frajka-Williams, E., Beaulieu, C. & Duchez, A. Emerging negative Atlantic Multidecadal Oscillation index in spite of warm subtropics. *Sci. Rep.* **7**, 1–8 (2017).
54. Rossby, T., Chafik, L. & Houpert, L. What can Hydrography Tell Us About the Strength of the Nordic Seas MOC Over the Last 70 to 100 Years? *Geophys. Res. Lett.* **47**, 1–9 (2020).
55. Yeager, S. G. & Robson, J. I. Recent progress in understanding and predicting Atlantic decadal climate variability. *Curr. Clim. Chang. Reports* **3**, 112–127 (2017).
56. Yashayaev, I. & Loder, J. W. Further intensification of deep convection in the Labrador Sea in 2016. *Geophys. Res. Lett.* **44**, 1429–1438 (2017).
57. Piron, A., Thierry, V., Mercier, H. & Caniaux, G. Gyre-scale deep convection in the subpolar North Atlantic Ocean during winter 2014. *Geophys. Res. Lett.* **44**, 1439–1447 (2017).

58. Gaillard, F., Reynaud, T., Thierry, V., Kolodziejczyk, N. & Von Schuckmann, K. In situ-based reanalysis of the global ocean temperature and salinity with ISAS: Variability of the heat content and steric height. *J. Clim.* **29**, 1305–1323 (2016).
59. Taburet, G. et al. DUACS~DT2018: 25~years of reprocessed sea level altimetry products. *Ocean Sci.* **15**, 1207–1224 (2019).
60. Kalnay, E. et al. The NCEP/NCAR 40-year reanalysis project. *Bull. Am. Meteorol. Soc.* **77**, 437–472 (1996).
61. Hogg, N. G., Pickart, R. S., Hendry, R. M. & Smethie, W. J. The northern recirculation gyre of the Gulf Stream. *Deep Sea Res. Part A. Oceanogr. Res. Pap* **33**, 1139–1165 (1986).
62. Geoffrey J. McLachlan & Krishnan Thriyambakam. *The EM Algorithm and Extensions, 2nd Edition*. (2008).
63. Maze, G. Ocean Profile Classification Model in python. (2020), https://doi.org/10.5281/ZENODO.3906236.

Acknowledgements

L.C. acknowledges support from the Swedish National Space Agency through the FiNNESS project (Dnr: 133/17). The authors gratefully acknowledge Bablu Sinha (National Oceanography Center, Southampton) for providing coding material for the tracer experiments. They acknowledge Martha Buckley for useful comments and suggestions to improve the original submission.

Author contributions

L.C. proposed the study and D.D. and L.C. designed it. D.D. implemented and performed the advective-diffusive model and the profile classification experiments. L.C. provided the satellite altimetry results. D.D., L.C., and G.M. analyzed the results. D.D. wrote the paper with contributions from all co-authors.

Competing interests

The authors declare no competing interests.

Additional information

Supplementary information The online version contains supplementary material available at https://doi.org/10.1038/s43247-021-00120-y.

Correspondence and requests for materials should be addressed to D.D.

Peer review information Primary handling editor: Heike Langenberg

Reprints and permission information is available at http://www.nature.com/reprints

Publisher's note Springer Nature remains neutral with regard to jurisdictional claims in published maps and institutional affiliations.

Open Access This article is licensed under a Creative Commons Attribution 4.0 International License, which permits use, sharing, adaptation, distribution and reproduction in any medium or format, as long as you give appropriate credit to the original author(s) and the source, provide a link to the Creative Commons license, and indicate if changes were made. The images or other third party material in this article are included in the article's Creative Commons license, unless indicated otherwise in a credit line to the material. If material is not included in the article's Creative Commons license and your intended use is not permitted by statutory regulation or exceeds the permitted use, you will need to obtain permission directly from the copyright holder. To view a copy of this license, visit http://creativecommons.org/licenses/by/4.0/.

© The Author(s) 2021